corrected Proof

Hydrology Research

Hydrology Research Vol 00 No 0, 1 doi: 10.2166/nh.2024.152

Flood susceptibility mapping in the Tongo Bassa watershed through GIS, remote sensing and frequency ratio model

Valentin Brice Ebodé *, Raphael Onguéné and Jean Jacques Braun

International Joint Laboratory DYCOFAC, IRGM-UY1-IRD, Yaounde, Cameroon
*Corresponding author. E-mail: ebodevalentinbrice@yahoo.fr

VBE, 0000-0003-3307-4789

ABSTRACT

Flooding constitutes a major problem for the inhabitants of Douala City in general and those of the Tongo Bassa watershed (TBW) in particular. Faced with this situation, public authorities need to put in place measures to mitigate the vulnerability of populations to these disasters. This article aims to map flooding risk areas in the TBW using the geographic information system, field data (historical flood points), remote sensing data (Sentinel II image) and the frequency ratio model. The map produced shows that 1.41, 8.88, 28.51, 33.86 and 27.33% of the basin area are respectively delimited into very low, low, medium, high and very high flood vulnerability classes. High and very high flooding risk areas (those where flooding is most likely to occur) occupy more than half of the basin (61.19%). These areas are characterized by significant imperviousness, low altitudes, weak slopes, significant proximity to watercourses and clayey soils. Most of the houses in the basin (66.92%) are located in areas affected by these two levels of exposure (high and very high). With respective success and prediction accuracy rates of 89 and 96.78%, a certain confidence deserves to be placed on the map of flooding risk areas produced.

Key words: flooding risk, frequency ratio model, GIS, remote sensing, Tongo Bassa

HIGHLIGHTS

- Flood susceptibility mapping is addressed through the geographic information system, remote sensing and the frequency ratio model.
- A flooding risk areas map with five levels of exposure is proposed.
- The number of houses included in each flood exposure level is summarized.

GRAPHICAL ABSTRACT

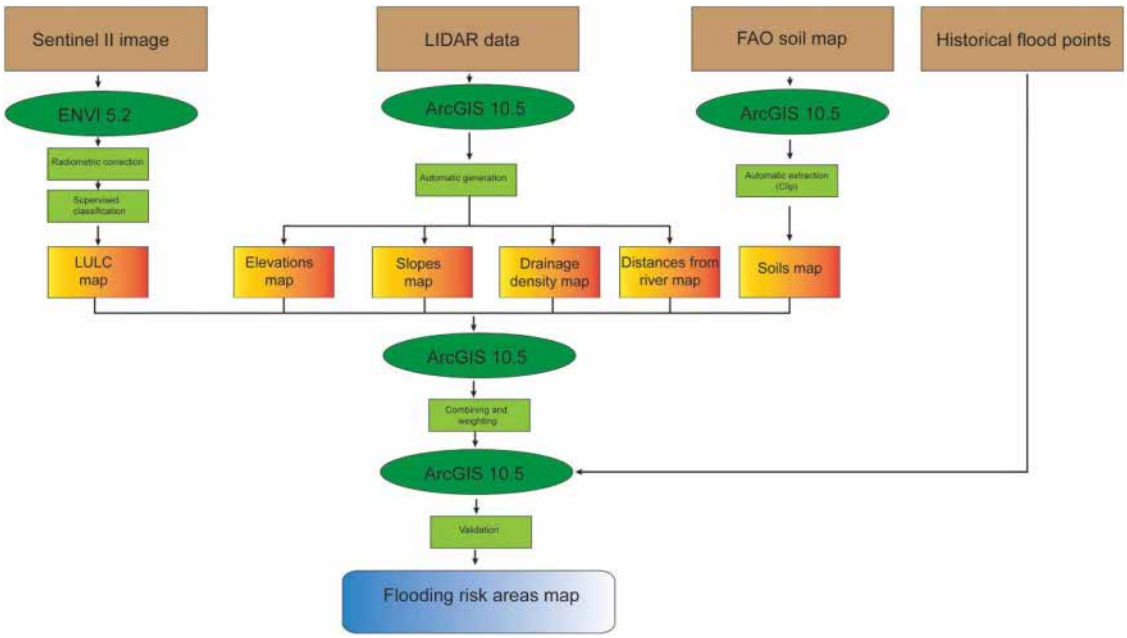

1. INTRODUCTION

Water resources management and related risks are increasingly becoming an important concern of contemporary society (Chomba *et al.* 2022; Ebodé 2022a; Ebodé *et al.* 2022; Nsangou *et al.* 2022). Among the wide range of existing hydrological risks, flooding appears to be one of the most devastating, considering the enormous damage it often causes (Samanta *et al.* 2018; Ekwueme 2022; Krisnayanti *et al.* 2022; Manzoor *et al.* 2022). Between the 1990s and 2010s, floods caused the deaths of more than 158,000 people around the world (Centre for Research on the Epidemiology of Disasters 2018). Economic losses of around $23 billion are also recorded due to floods each year (UN 2018). If we stick to climate forecasts and changes in land use and land cover (LULC) patterns, we will observe an increase in the number and territories exposed to these disasters (Vidhee & Amit 2020; Asinya & Alam 2021; Chen *et al.* 2023).

In the European Union, flood phenomena were responsible for one-third of the economic losses caused by natural disasters between 1980 and 2016 (Costache *et al.* 2020). In terms of the loss of human lives and destruction of property, floods are among the most widespread and severe natural hazards in this region (Costache *et al.* 2020). The amount of damage due to the California floods in 1997 was $2,000 million. That of Mississippi in 1995 was $7,499 million. Environmentally, Nsangou *et al.* (2022) reported the Indian Himalaya in 2013 witnessed the terrible event of the Kedarnath flash flood, which was very disastrous and tragic, resulting in a serious stage modification of some geomorphological units in the watershed. Finally, for the African continent alone, the costs could amount to several billions of euros for insurers (Nsangou *et al.* 2022). Thus, the human desire to build in flooding areas risk appears in flagrant contradiction with the current phenomenon of flooding risk increase, which threatens many human lives and infrastructure (socio-economic, heritage, etc.).

Compared to other parts of the world, sub-Saharan Africa seems more vulnerable to these disasters due to poverty, poor governance and low technological level (Ahouangan *et al.* 2010). In the case of Cameroon, a study published by Centre for Research on the Epidemiology of Disasters (2016) states that 367,276 people were affected by floods between 2007 and 2015. Douala City is the most affected area due to its flat terrain, its exponential demographic growth (which leads to an anarchic occupation of spaces, including those reserved for the water circulation) and its proximity to the Atlantic Ocean, which is the origin of tidal phenomena. Between 2000 and 2010, floods caused more than 100 deaths and significant material damage in Douala City.

The fight against flooding begins with detailed and precise mapping of risk areas (Tehrany *et al.* 2015; Ebodé 2022b). Geographic information system (GIS) and remote sensing (RS) techniques and data have largely contributed to the analysis of natural hazards (Jaafari *et al.* 2014; Moel *et al.* 2014). Many studies relating to flooding risk area mapping have been carried

out using GIS (Strobl *et al.* 2012; Pradhan *et al.* 2014). Among the most popular approaches in natural hazard modelling, we have frequency ratio (FR) (Tehrany *et al.* 2015; Samanta *et al.* 2018), analytical hierarchy process (Stefanidis & Stathis 2013), fuzzy logic, logistic regression, artificial neural networks (Kia *et al.* 2012; Lohani *et al.* 2012) and weights of evidence (Dahal *et al.* 2008). Among all these approaches, the FR could be considered one of the simplest and most effective in flooding risk area mapping (Liao & Carin 2009). It is a relatively new tool widely used for risk areas mapping several other complex natural disasters, such as landslides (Rahmati *et al.* 2016). These different reasons led us to adopt this approach in this study.

The Tongo Bassa watershed (TBW) is the largest and most populated in Douala City. Even though it is one of the basins most affected by flooding, the Tongo Bassa has so far only been the subject of a very small number of relevant works on this issue (Elong *et al.* 2022; Sone *et al.* 2023). In these works, the FR model has never been used despite its effectiveness and simplicity. Also, the mapping of homes located in areas corresponding to each level of exposure to flooding (very low, low, medium, high and very high) has never been addressed in the few existing studies carried out in this basin, despite the importance it has for decision-making during development and for prioritizing interventions in the event of a hazard.

This study therefore aims to (1) validate the FR model in the TBW and the region; (2) produce a reliable map of flooding risk areas in the TBW with this model and (3) map homes included in each level of exposure (very low, low, medium, high and very strong). The third objective was not easily achieved due to the difficulty of accessing key information, allowing us to go further in the analysis than the few existing studies (distribution of houses in the basin). These data make it possible to propose additional, more concrete tools for development (maps of homes included in the flooding risk area and whose occupants should be relocated to appropriate sites). These data were extracted from Google Earth.

2. MATERIALS AND METHODS

2.1. Study area

The TBW is the largest and one of the most active on economic plans in Douala City (the economic capital of Cameroun). This cosmopolitan city of around 3 million inhabitants concentrates nearly 20% of the country's urban population and is the most populous city in Central Africa. The port of Douala is the main gateway to Cameroon and indeed the Central African sub-region, and serves several neighbouring countries. Delimited at its outlet located at the confluence with the Wouri (Figure 1), the TBW has an area of approximately 44.12 km^2. Oriented East-West, this town (Douala) is located between 4°2′0″ and 4°5′30″ North latitude and between 9°43′0″ and 9°47′20″ East longitude (Figure 1). Its hydrographic network

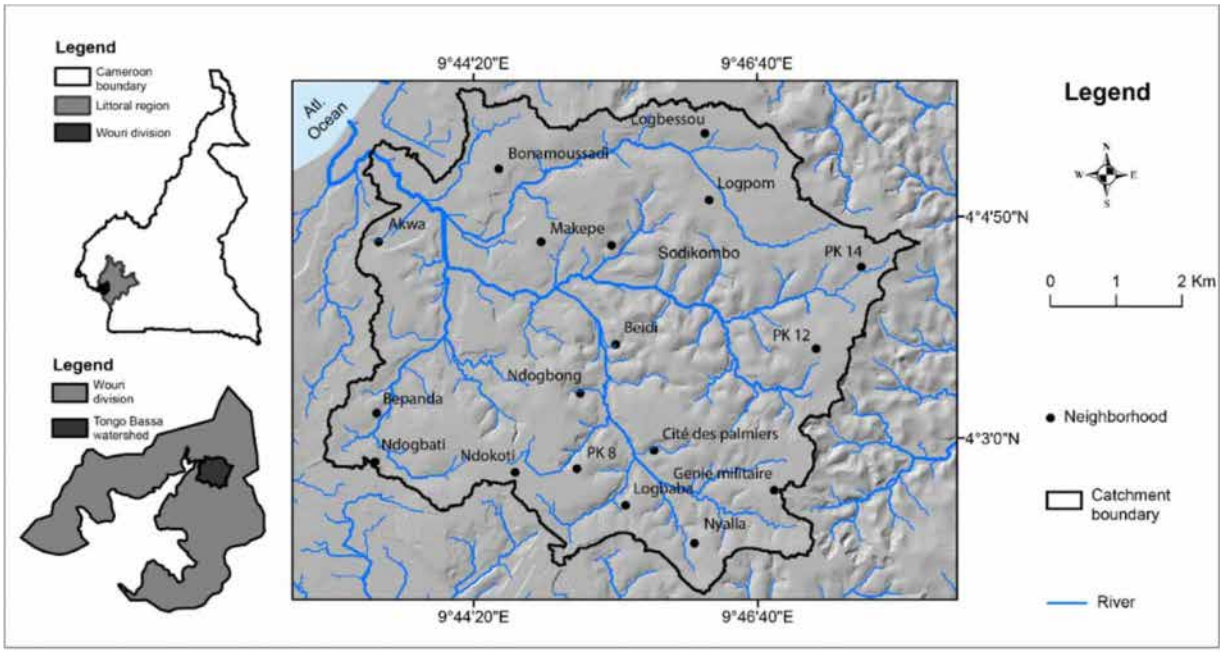

Figure 1 | Location map of the TBW.

is dendritic. The climate there is hot and humid equatorial, with temperatures between 21 and 36°C, and abundant annual precipitation (3,593 mm on average) (Ebodé 2022c). This precipitation falls during a single season, which extends from March to November. Geologically, the TBW is dominated by Mio-Pliocene sandy formations, which are favourable to infiltration and rapid waterlogging of soil (Boum-Nkot *et al.* 2015). These formations are covered by ferralitic soils, predominantly yellowish and sometimes variegated sandy-clayey. On these soils, vegetation grows, mainly consisting of mangrove forests. Relief presents a relatively monotonous appearance in this basin.

2.2. Data sources

The data used in this study include a Sentinel II satellite image, a digital terrain model (light detection and ranging (LIDAR) data), the Food Agriculture Organization (FAO) soil map and historical flooding points (Table 1 and Figure 2). These data made it possible to obtain six independent variables (LULC patterns, altitudes, slopes, distance from watercourses, drainage densities and soil types) (Figure 2), which were subsequently crossed to generate a map of flooding risk areas of the investigated basin. These different variables are considered by some authors (Costache *et al.* 2020; Nsangou *et al.* 2022) to be the main factors in the occurrence of floods in a given region since they influence runoff and water infiltration.

2.3. Data analysis

Supervised classification by maximum likelihood made it possible to produce a map of the main LULC patterns of the basin using ENVI 5.2 software. This operation was preceded by preprocessing and object recognition operations in the field using photography and global positioning system (GPS). Preprocessing of satellite images refers to all the processes applied to raw

Table 1 | Data used for the mapping of flooding risk areas in the TBW

Data	Use	Scale	Sources
Sentinel II satellite image	LULC map	10 m	Earth Explorer
LIDAR data	Maps of elevations, slopes, stream distances and drainage densities	10 m	Urban community of Douala
FAO soil map	Soil map	1/500,000	FAO
Historical flood points	Realization and validation of the flooding risk areas map	–	Urban community of Douala

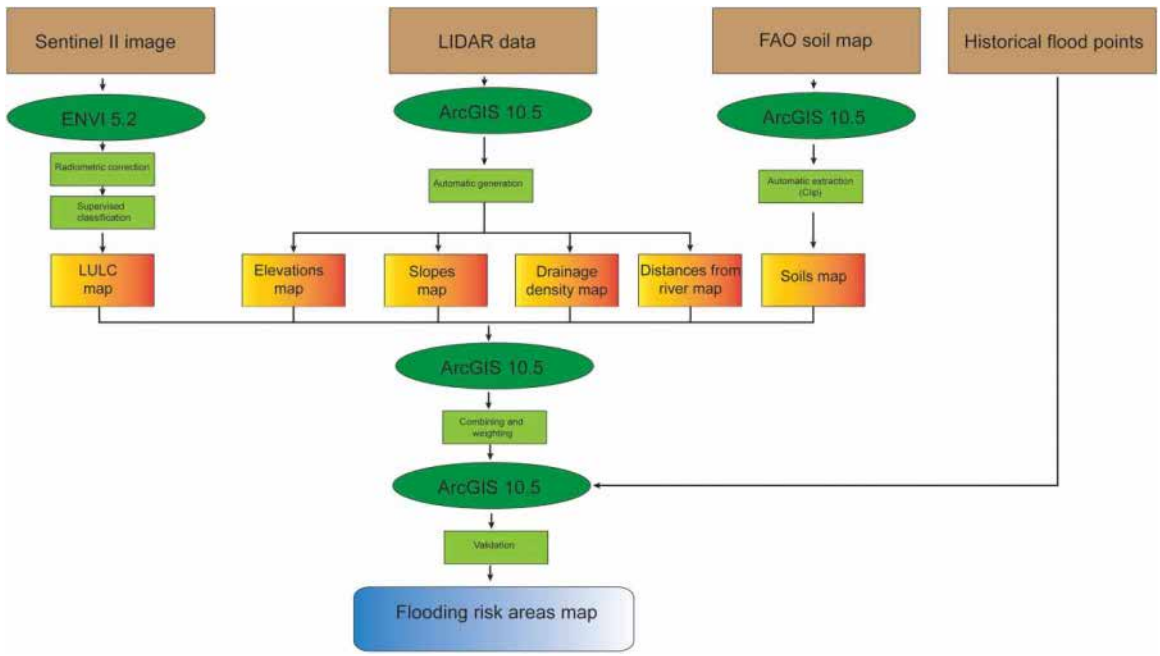

Figure 2 | Study workflow.

data to correct geometric and radiometric errors that characterize some satellite images (Ebodé 2023). These errors are generally due to technical problems with satellites and interactions between outgoing electromagnetic radiation and atmospheric aerosols, also called 'atmospheric noise'. The downloaded Sentinel II image being orthorectified, the preprocessing concerned the atmospheric correction of this image and its reprojection into the local system (WGS_84_UTM_Zone_32N). For this, neochannels are created to increase the readability of the data by enhancing less obvious properties in the original image, thus showing the scene elements more clearly. Three indices are therefore created, namely normalized difference vegetation index (NDVI), brightness index (BI) and normalized difference water index (NDWI). We chose these indices because they respectively highlight vegetated surfaces and sterile (non-chlorophyll) elements such as urban areas and water bodies. This allowed us to make much more precise supervised classifications (close to reality). Their formulas are as follows:

$$\mathrm{NDVI} = \frac{\mathrm{NIR} - R}{\mathrm{NIR} + R} \tag{1}$$

$$\mathrm{BI} = (R^2 + \mathrm{NIR}^2)^{0.5} \tag{2}$$

$$\mathrm{NDWI} = \frac{\mathrm{NIR} - \mathrm{MWIR}}{\mathrm{NIR} + \mathrm{MWIR}} \tag{3}$$

Where NIR is the surface ground reflectance in the near-infrared channel; R is the ground reflectance of the surface in the red channel and MWIR is the ground reflectance of the surface in the mid-infrared channel. The use of Google Earth, as well as the areas sampled from GPS, made it possible to identify with certainty impervious areas (built-up areas, savannahs, bare soils and crops), water bodies (large rivers, lakes and ponds) and forests. Before classification operation, the separability of the spectral signatures of the sampled objects to avoid interclass confusion was evaluated, by calculating the 'transformed divergence' index. The value of this index is between 0 and 2. A value > 1.8 indicates good separability between two given classes. The different classes used in this study show good separability between them, with indices >1.9.

Maps of altitudes, slopes, drainage densities and distances of watercourses were automatically generated using ArcGIS 10.5 software. The soil map of the basin was extracted from the FAO world soil map. Mapping historical flood points is also essential for determining flooding risk areas. In total, 231 historical flood points were used for the calibration and validation of the FR model selected for this study. This model establishes the relationship between the occurrence of flooding and various variables recognized as causing flooding. The values of the FR indices are calculated according to the formula:

$$\mathrm{FSI} = \sum \mathrm{FR} \tag{4}$$

where FSI and FR are, respectively, the flood susceptibility index and the frequency ratio for each factor/variable.

The FR is the ratio of the flooded area to the total study area, which demarcates the flooded area from the non-flooded area (Samanta *et al.* 2018). It is calculated according to the formula:

$$\mathrm{FR} = \frac{(E/F)}{(M/L)} \tag{5}$$

where E is the number of floods for each factor/variable; F is the total number of floods; M is the area of each factor and L is the total area of the study area.

The FR values indicate the types of correlation between different factors and flooding. A FR value greater than 1 indicates a strong correlation with flooding; on the other hand, a value less than 1 indicates a weak correlation with flooding. Table 2 shows the value of the FR of each of the classes of different variables.

To obtain the flooding risk area map, all variables are converted to raster format. The spatial resolution of each of the rasters was defined on a cell size of 10×10 m, and it is integrated into the ArcGIS database. This integrated database has been reclassified into five classes of flood sensitivity, namely very low, low, medium, high and very high.

Table 2 | Variables used for determining flooding risk areas from the FR model

Independent variables	Classes	Areas (km^2)	Basin occupancy rate (%)	Number of floods	FR
LULC	Built and road	36.4	82.5	173	**1.04**
	Bare soil and crop	6.6	14.95	23	0.76
	Forest	1	2.28	3	0.6
	Water	0.12	0.27	1	**1.83**
Altitudes (m)	−1 to13	9.22	20.89	188	**4.49**
	14–25	12.4	28.1	12	0.21
	26–37	10.5	23.82	0	0
	38–57	12	27.19	0	0
Slopes (%)	0–3	24	54.39	107	**1.01**
	4–7	13	29.46	51	0.86
	8–14	5.7	12.94	27	**1.04**
	15–42	1.42	3.21	15	**2.33**
Drainage density (km/km^2)	44–53	7	15.86	18	0.56
	54–63	28.8	65.29	147	**1.12**
	64–72	7.7	17.45	22	0.63
	73–82	0.62	1.4	13	**4.62**
Distance from rivers (m)	0–142	23.7	53.71	184	**1.71**
	143–283	14.7	33.31	16	0.24
	284–425	5	11.35	1	0.04
	426–567	0.72	1.63	0	0
Soils	Fx1-1a-583 (Sandy-loamy)	19.92	45.14	0	0
	J4-a-674 (Clayey)	24.2	54.86	200	**1.82**

3. RESULTS AND DISCUSSION

3.1. Links between independent variables and flood occurrence

The six variables retained for flooding risk areas mapping in this study each include several classes (Table 2 and Figures 3–8). Four classes appear on the LULC map, notably buildings and roads, bare soil and crops, forests and water bodies (Figure 3). Among these classes, only water bodies (0.27% of the basin) and buildings (82.5% of the basin) are well correlated with flooding. Their FRs are 1.83 and 1.04, respectively (Table 2). The FRs of the other two classes are less than 1.

As in the case of LULC patterns, the altitudes of the basin have been reclassified into four categories (–1 to 13 m; 14–25 m; 26–37 m and 38–57 m) (Figure 4). Only the –1 to 13 m class (20.89% of the total basin surface) is well correlated with flooding, with a significant FR of 4.49 (Table 2).

The slopes of the basin were also divided into four classes (0–3%; 4–7%; 8–14% and 15–42%) (Figure 5). Only the 4–7% slope class is poorly correlated with flooding. The other three classes are well correlated with flooding. Their FRs are greater than 1 (Table 2). The most important FR is that of the class of slopes 15–47%, which occupy 3.21% of the total area of the basin (Table 2).

The drainage densities of the basin are divided into four classes (44–53 km/km^2; 54–63 km/km^2; 64–72 km/km^2 and 73–82 km/km^2; Figure 6). Two of them (54–63 km/km^2 and 73–82 km/km^2) appear to be well correlated with flooding, with respective FRs of 1.12 and 4.62, and respective basin occupancy rates of 65.29 and 1.4% (Table 2).

Four classes (0–142 m; 143–283 m; 284–425 m and 426–567 m) also appear on the map of distances to watercourses (Figure 7). The 0–142 m class, whose basin occupancy rate is 53.71%, is the only one for which the FR is greater than 1 (Table 2).

The soils of the investigated basin are divided into only two classes (sandy-loamy and clayey) (Figure 8). Unlike sandy-loamy soils, clayey soils (54.86% of the basin) are well correlated with flooding, with a FR of 1.82 (Table 2).

3.2. Flooding risk areas mapping

The FR values calculated for each parameter vary between 0 and 4.62 in the study area (Table 2). A FR value less than 1 indicates a weak correlation with flooding and the opposite otherwise (Lee *et al.* 2012). Subsequently, a flood susceptibility

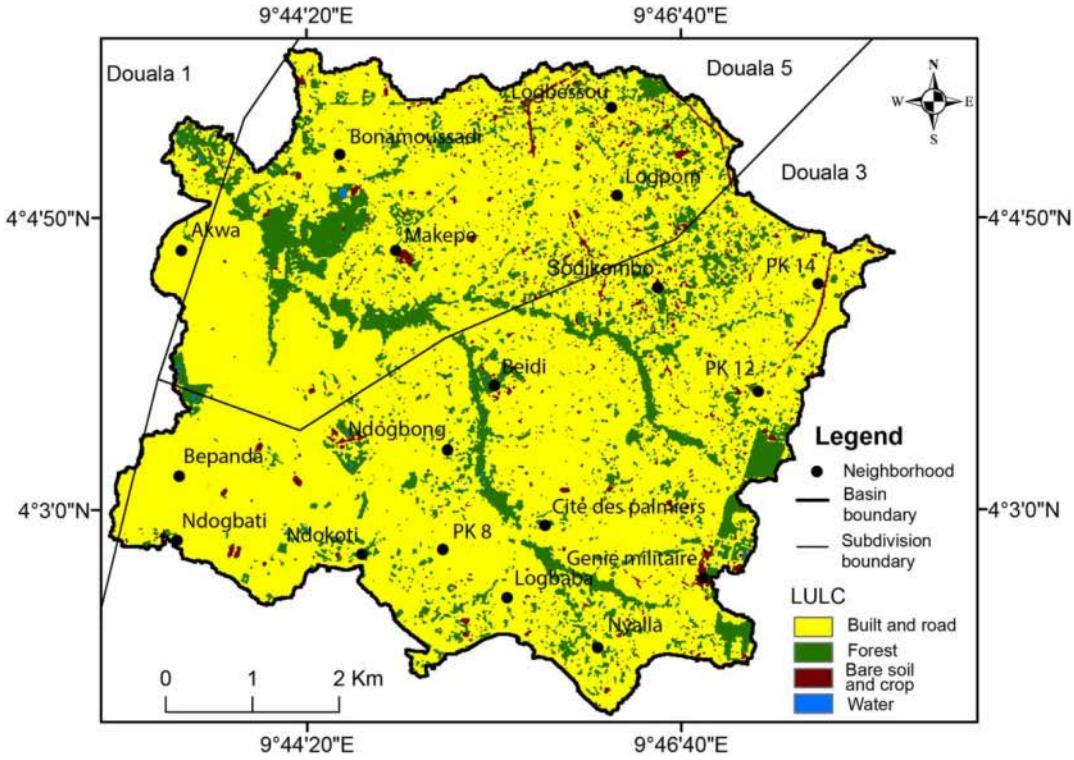

Figure 3 | Spatial distribution of the main LULC patterns in the TBW.

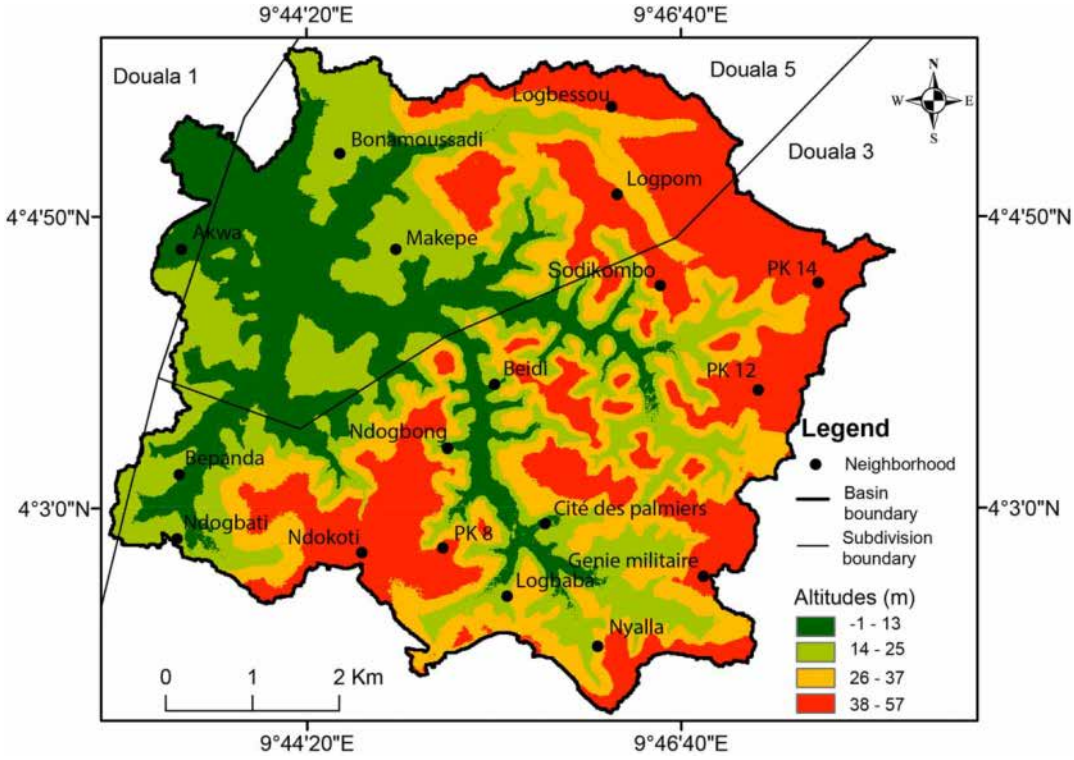

Figure 4 | Elevations map of the TBW.

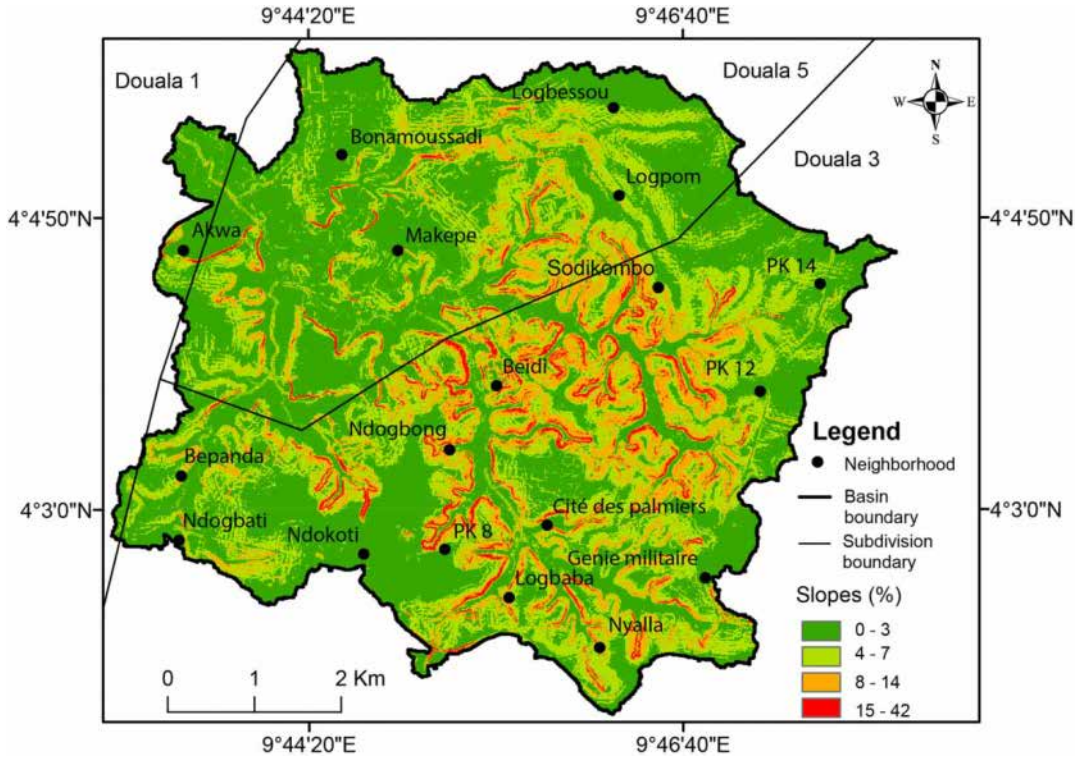

Figure 5 | Slopes map of the TBW.

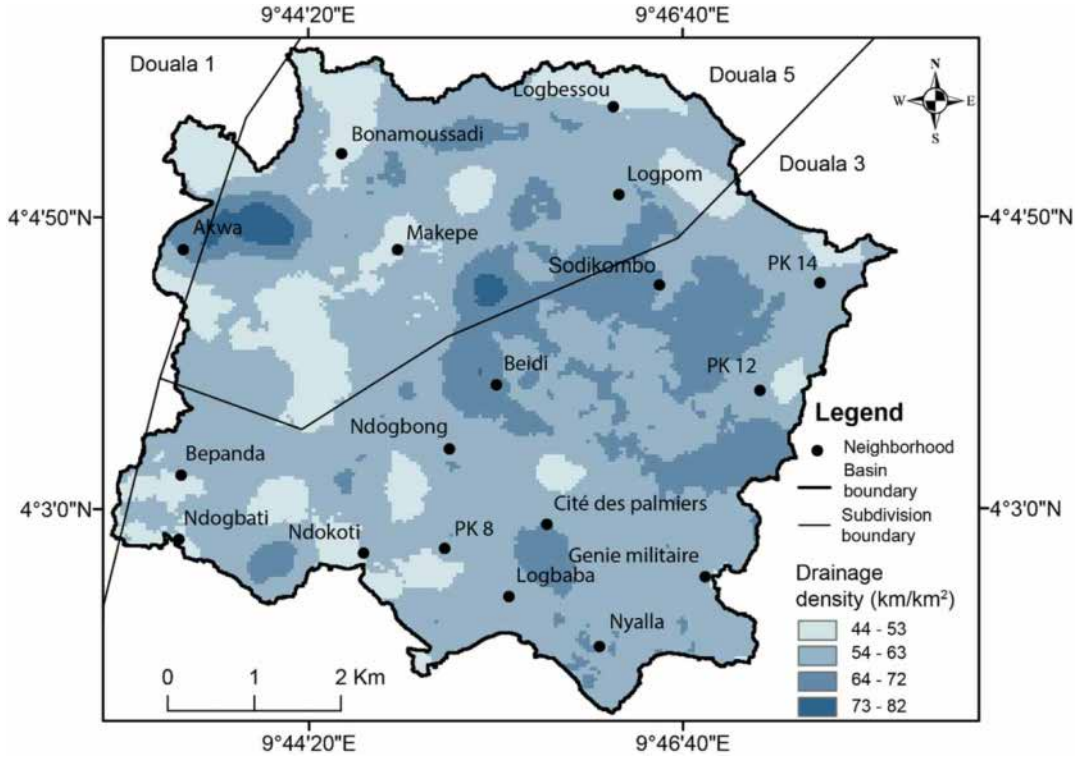

Figure 6 | Drainage densities map of the TBW.

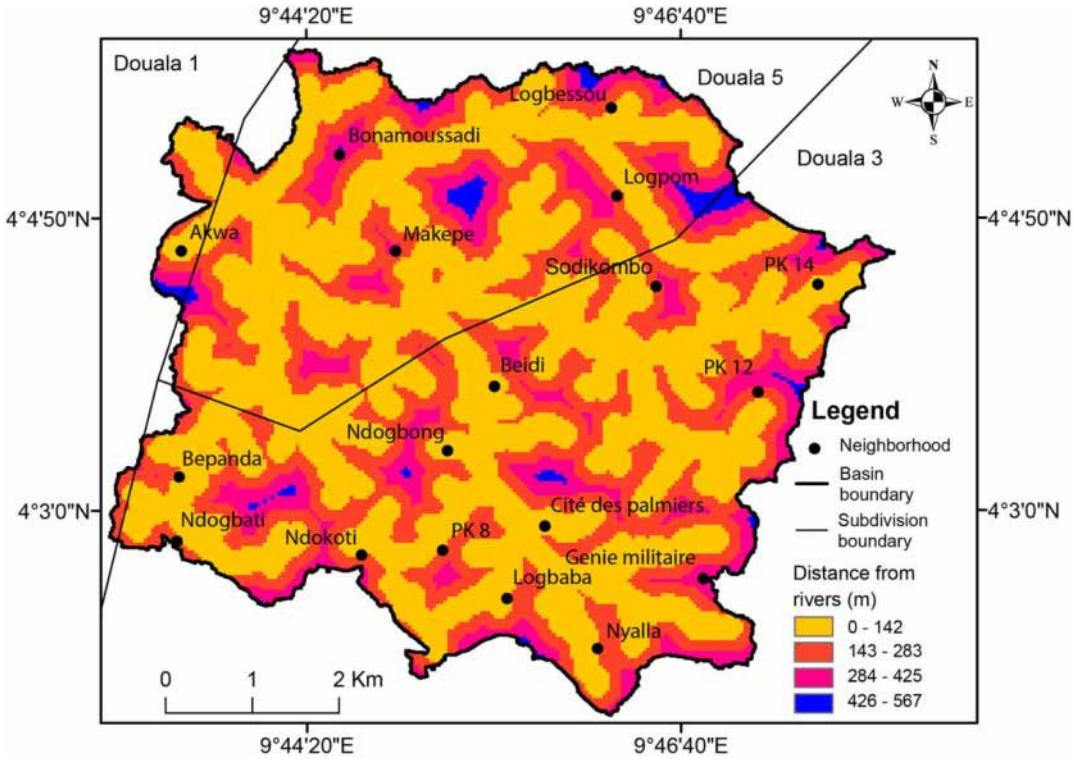

Figure 7 | Distance from rivers map of the TBW.

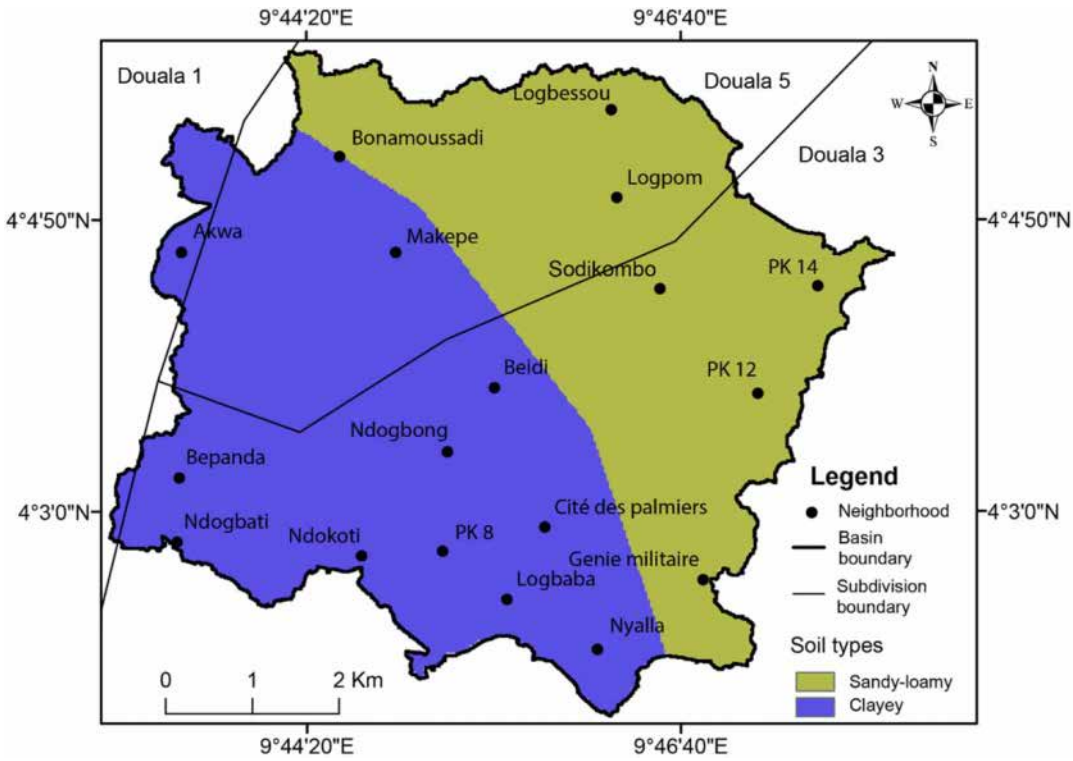

Figure 8 | Soils map of the TBW.

database was developed using the FR model equation (Equation (4)). The database created was reclassified into five flood sensitivity categories, namely very low, low, medium, high and very high. Figure 9 shows the flood sensitivity classes. Flood sensitivity analysis indicates that 1.41, 8.88, 28.51, 33.86 and 27.33% of the basin area are, respectively, demarcated into very low, low, medium, high and very high flood vulnerability classes (Table 3).

High and very high flooding risk areas are where flooding is most likely to occur. They are characterized by significant imperviousness, low altitudes, weak slopes, significant proximity to watercourses and clayey soils.

It has already been shown in other studies around the world that low altitudes and slopes, proximity to watercourses and imperviousness present the most important links with flooding (Esteves 2013; Colmet-Daage *et al.* 2017; Sone *et al.* 2023).

3.3. FR model validation

To validate the FR model, it is important to calculate the success rate and accuracy of the predictions. The success rate was calculated using 200 historical flood points. The prediction accuracy was calculated using 31 historical flood points. Future flooding is most likely to occur in areas with high and very high flood risk (Samanta *et al*. 2018). The success and accuracy rates of the predictions are 89 and 96.78% (Table 3). Such prediction accuracy validates the FR model in the studied watershed and proves at the same time that it is suitable for flooding risk areas mapping in the studied region.

As is the case in this study, the FR model has already been used to reliably map flooding risk areas in other basins around the world (Liao & Carin 2009; Pradhan & Youssef 2011; Lee *et al.* 2012; Samanta *et al*. 2018).

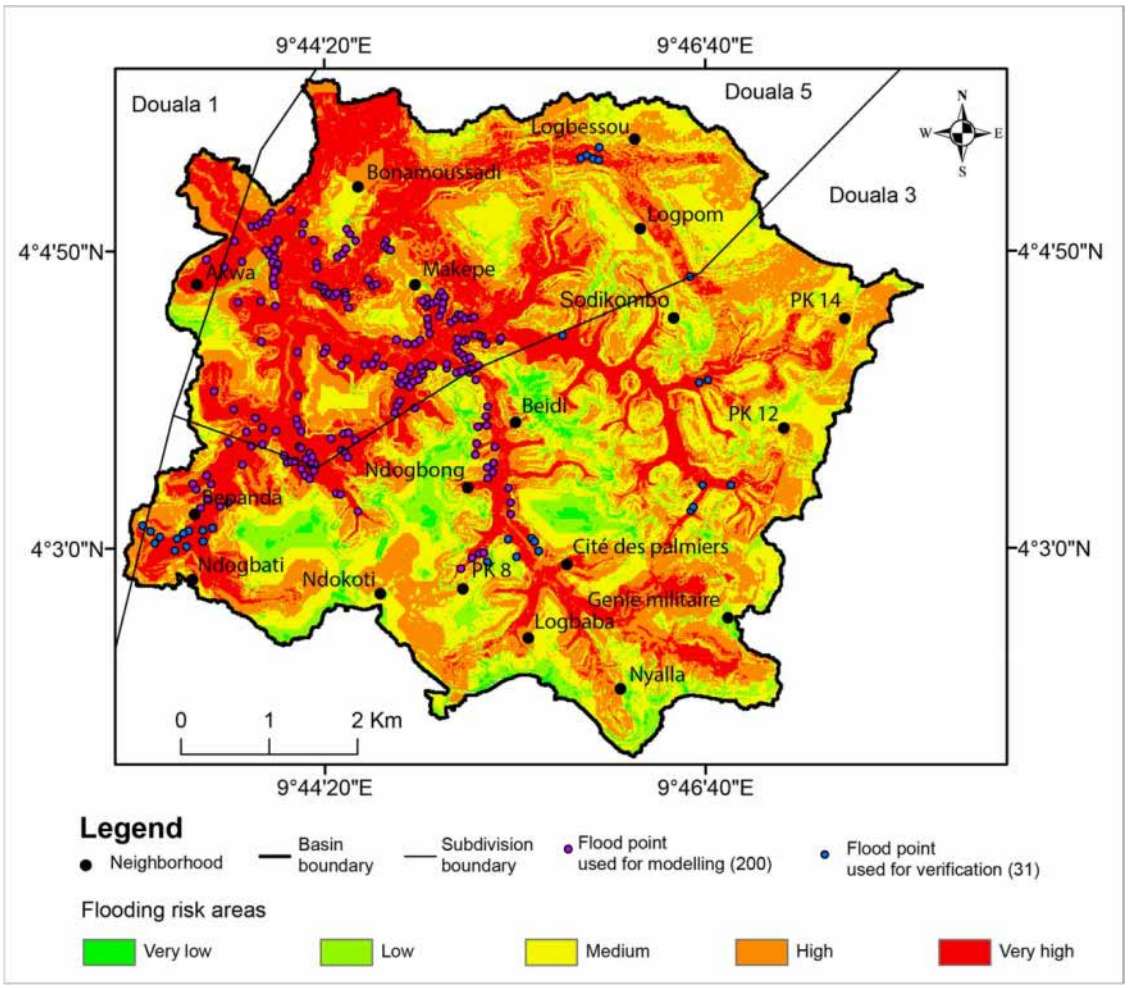

Figure 9 | Map of flooding risk areas in the TBW.

Table 3 | Statistics relating to the spatial distribution and degree of precision of flooding risk areas in the TBW

Flood risk areas	Areas (km²)	Basin occupancy rate (%)	Flood points used for modelling (200)		Flood points used for validation (31)	
			Number	%	Number	%
Very low	0.62	1.41	0	0.00	0	0.00
Low	3.92	8.88	3	1.50	0	0.00
Medium	12.58	28.51	19	9.50	1	3.22
High	14.94	33.86	50	25.00	5	16.13
Very high	12.06	27.33	128	64.00	25	80.65
Total	44.12	100.00	200	100.00	31	100.00
Total precision (%)	–	–	–	89	–	96.78

Note: The calculation of the total degree of accuracy only includes the areas with high and very high flooding risk.

3.4. Quantity of houses included in each flood exposure level

The exposure levels which include the greatest number of houses are in the following order: high (25,712 houses or 38.5%), medium (20,509 houses or 30.72%), very high (16,268 houses or 24.42%), low (2,835 houses or 4.24%) and very low (1,418 or 2.12%) (Table 4). Most of the houses included in the flooding zone are located to the South and Southwest of the basin, regardless of the exposure level. More than half of the houses in the basin are located in high and very high-risk zones (41,980 houses or 62.92%), which are the exposure levels with the greatest impacts for which measures must be taken.

Most authors who have dealt with flooding in their work generally limit themselves to producing a map of risk areas using various methods (Chen *et al.* 2011; Lohani *et al.* 2012; Zou *et al.* 2013; Haghizadeh *et al.* 2017). The rate of houses included in each exposure level (very low, low, medium, high and very high) is a dimension of analysis that is missing in this work. However, this information can help to get an idea of the impact level of flooding on the populations of a given basin and the prioritization of interventions during different hazards. It can indeed happen that the zone at high risk of flooding has a large surface area in a basin, but that the population is mainly settled in the zones at medium and low risk. This reflects the low vulnerability of the population to flooding. On the other hand, if the majority of the population is settled in areas with a high and very high flooding risk, as is the case in this study, this implies high vulnerability and therefore, urgent decision-making. It is crucial to always cross information relating to the different levels of exposure with that of houses to get a clear idea of the current degree of vulnerability of the different parts of a given area and thus be able to prioritize interventions in the event of a hazard.

4. CONCLUSION

This study aimed to map flooding risk areas in the TBW using the GIS technique, field data (historical flood points), RS (Landsat image) data and the FR model. For this, six independent variables influencing floods were retained (LULC patterns, altitudes, slopes, drainage densities, distances from watercourses and soil types). At its end, it appears that areas with high and very high risk of flooding (those where flooding is most likely to occur) occupy more than half of the basin. Their respective

Table 4 | Number of houses included in each exposure level

Flood risk areas	Number of houses	%
Very low	1,418	2.12
Low	2,835	4.24
Medium	20,509	30.72
High	25,712	38.5
Very high	16,268	24.42
Total	66,742	100

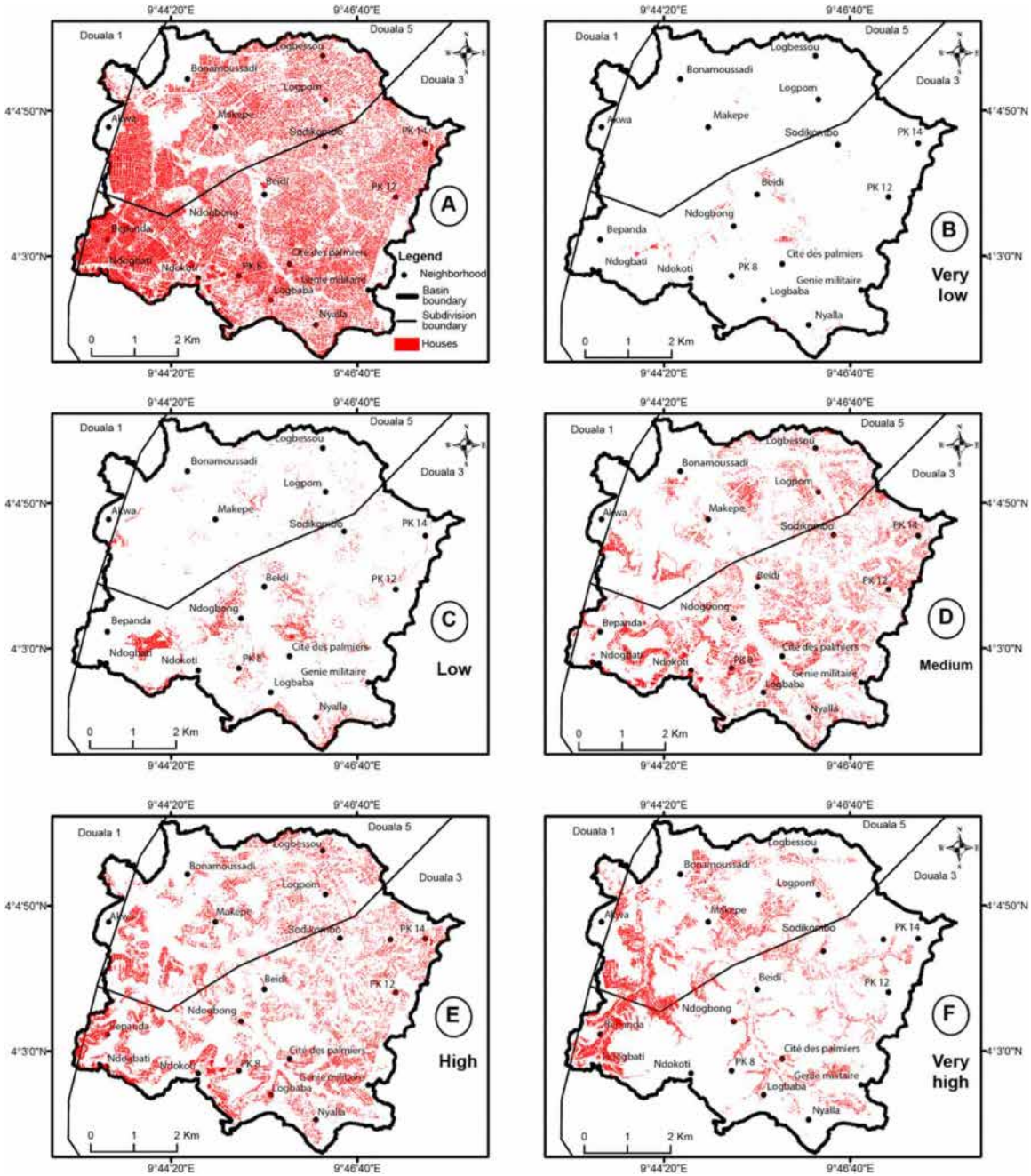

Figure 10 | Spatial distribution of houses included in the studied basin in 2022 and in the different flood risk areas (B: very low; C: low; D: medium; E: high and F: very high).

basin occupancy rates are 33.86 and 27.33%. These areas are characterized by significant imperviousness, low altitudes, weak slopes, significant proximity to watercourses and clayey soils. Most of the houses in the basin (66.92%) are located in areas affected by these two levels of exposure (high and very high) (Figure 10). With respective success and prediction accuracy rates of 89 and 96.78%, the map of flood risk zones produced for the investigated basin deserves a certain amount of confidence to be placed in it. This tool can be validly used by the public authorities to fight against flooding in this basin. Although the results of this study are satisfactory overall, the inclusion of some key parameters, such as geology, would have made it possible to have significantly better results. Field studies are necessary to have a complete database on this basin and the region, which would make it possible to further refine the analyses in such studies.

DATA AVAILABILITY STATEMENT

All relevant data are included in the paper or its Supplementary Information.

CONFLICT OF INTEREST

The authors declare there is no conflict.

REFERENCES

Ahouangan, B., Houinato, M., Ahamide, B., Agbossou, E. & Sinsin, B. 2010 Etude comparative de la productivité de repousses et de la capacité de charge des hémicryptophytes soumises aux feux de végétation dans les parcelles irriguées et non irriguées dans la Réserve Transfrontalière de Biosphère (RTB) du W-Benin. *International Journal of Biological and Chemical Sciences* **4**, 2.

Asinya, A. E. & Alam, M. J. 2021 Flood risk in rivers: Climate driven or morphological adjustment. *Earth Systems and Environment*. doi:10.1007/s41748-021-00257-y.

Boum-Nkot, N., Ketchemen-Tandia, B., Ndje, Y., Emvouttou, H., Ebonji, C. R. & Huneau, F. 2015 Origin of mineralization of groundwater in the Tongo Bassa Watershed (Douala-Cameroon). *Research Journal of Environmental and Earth Sciences* **7** (2), 29–41.

Chen, Y. R., Yeh, C. H. & Yu, B. 2011 Integrated application of the analytic hierarchy process and the geographic information system for flood risk assessment and flood plain management in Taiwan. *Natural Hazards* **59** (3), 1261–1276.

Chen, J., Shi, X., Gu, L., Wu, G., Su, T., Wang, H., Kim, J., Zhang, L. & Xiong, L. 2023 Impacts of climate warming on global floods and their implication to current flood defense standards. *Journal of Hydrology* **618**, 129236. doi:10.1016/j.jhydrol.2023.129236.

Chomba, I., Banda, K., Winsemius, M., Sichingabula, H. & Nyambe, I. 2022 Integrated hydrologic-hydrodynamic inundation modeling in a groundwater dependent tropical floodplain. *Journal of Human, Earth, and Future* **3**, 2. doi:10.28991/HEF-2022-03-02-09.

Colmet-Daage, A., Cécile, L., Borrell-Estupina, V., Servat, E., Gomez, E. S. & Ricci, S. 2017 Climate change impacts on extreme rainfalls, discharges and floods in Mediterranean catchments. In *IAHS 2017 Scientific Assembly*, July 2017, Port Elizabeth, South Africa. ⟨hal-02104194⟩.

Costache, R., Ţîncu, R., Elkhrachy, I., Pham, Q., Popa, C., Diaconu, D., Avand, M., Costache, I., Arabameri, I. & Bui, T. 2020 New neural fuzzy-based machine learning ensemble for enhancing the prediction accuracy of flood susceptibility mapping. *Hydrological Sciences Journal* **65** (16), 2816–2837. doi:10.1080/02626667.2020.1842412.

Centre for Research on the Epidemiology of Disasters 2016 *Poverty & Death: Disaster Mortality, 1996–2015*. Centre for Research on the Epidemiology of Disasters, Brussels, Belgium.

Centre for Research on the Epidemiology of Disasters 2018 *Natural Disasters in 2018: Lower Mortality, Higher Cost*. CRED crunch, N° 29: 2018, p. 6.

Dahal, R., Hasegawa, S., Nonomura, A., Yamanaka, M., Masuda, T. & Nishino, K. 2008 Modélisation des poids de la preuve basée sur le SIG des glissements de terrain induits par les précipitations dans de petits bassins versants pour la cartographie de la sensibilité aux glissements de terrain. *Environmental Geology* **54**, 311–324.

Ebodé, V. B. 2022a Impact of rainfall variability and land-use changes on river discharge in Sanaga catchment (forest–savannah transition zone in Central Africa). *Hydrology Research* **53** (7), 1017. doi:10.2166/nh.2022.046.

Ebodé, V. B. 2022b Hydrological variability and flood risk in a forest watershed undergoing accelerated urbanization: The case of Mefou (South Cameroon). *Water Supply* **22** (12), 8778. doi:10.2166/ws.2022.398.

Ebodé, V. B. 2022c Analysis of the spatio-temporal rainfall variability in Cameroon over the period 1950 to 2019. *Atmosphere* **13**, 1769. doi:10.3390/atmos13111769.

Ebodé, V. B. 2023 Impact of climate and anthropogenic changes on current and future variability in flows in the Nyong River Basin (equatorial Central Africa). *Journal of Hydroinformatics* **25** (2), 369. doi:10.2166/hydro.2023.116.

Ebodé, V. B., Dzana, J. G., Nkiaka, E., Nka, N. B., Braun, J. J. & Riotte, J. 2022 Effects of climate and anthropogenic changes on current and future variability in flows in the So'o River Basin (south of Cameroon). *Hydrology Research* **53** (9), 1203–1220. doi:10.2166/nh.2022.047.

Ekwueme, B. N. 2022 Machine learning based prediction of urban flood susceptibility from selected rivers in a tropical catchment area. *Civil Engineering Journal* **8**, 9. doi:10.28991/CEJ-2022-08-09-08.

Elong, A. J., Zhou, L., Karney, B., Fang, H., Cao, Y. & Assam, S. L. Z. 2022 Flood prediction with two-dimensional shallow water equations: A case study of Tongo-Bassa watershed in Cameroon. *Applied Science* **12**, 11622. doi:10.3390/app122211622.

Esteves, L. S. 2013 Consequences to flood management of using different probability distributions to estimate extreme rainfall. *Journal of Environment Management* **115**, 98–105.

Haghizadeh, A., Siahkamari, S., Haghiabi, A. H. & Rahmati, O. 2017 Forecasting flood-prone areas using Shannon's entropy model. *Journal of Earth System Science* **126**, 39. doi:10.1007/s12040-017-0819-x.

Jaafari, A., Najafi, A., Pourghasemi, H., Rezaeian, J. & Sattarian, A. 2014 Rapport de fréquence basé sur SIG et indice des modèles d'entropie pour l'évaluation de la sensibilité aux glissements de terrain dans la forêt caspienne, nord de l'Iran. *International Journal of Environmental Science and Technology* **11**, 909–926.

Kia, M., Pirasteh, S., Pradhan, B., Rodzi, M., Sulaiman, W. & Moradi, A. 2012 An artificial neural network model for flood simulation using GIS: Johor River Basin, Malaysia. *Environmental Earth Sciences* **67**, 251–264.

Krisnayanti, D., Rozari, P., Garu, V., Damayanti, A., Legono, D. & Nurdi, H. 2022 Analysis of flood discharge due to impact of tropical cyclone. *Civil Engineering Journal* **8**, 9. doi:10.28991/CEJ-2022-08-09-01.

Lee, M. J., Kang, J. E. & Jeon, S. 2012 Application of frequency ratio model and validation for predictive flooded area susceptibility mapping using GIS. In *Proceedings of Geoscience and Remote Sensing Symposium (IGARSS), 2012 IEEE International*. Munich, pp. 895–898.

Liao, X. & Carin, L. 2009 Migratory logistic regression for learning concept drift between two data sets with application to UXO sensing. *IEEE Transactions on Geoscience and Remote Sensing* **47**, 1454–1466.

Lohani, A., Kumar, R. & Singh, R. 2012 Hydrological time series modeling: A comparison between adaptive neuro-fuzzy, neural network and autoregressive techniques. *Journal of Hydrology* **442**, 23–35.

Manzoor, Z., Ehsan, M., Khan, M., Manzoor, A., Akhter, M., Sohail, M., Hussein, A. & Shafi, A. 2022 Floods and flood management and its socio-economic impact on Pakistan: A review of the empirical literature. *Frontiers in Environmental Science* **10**. doi:10.3389/fenvs.2022.1021862.

Moel, H. D., Vliet, M. & Aerts, J. 2014 Évaluation de l'effet des mesures de réduction des dommages causés par les inondations: Une étude de cas de la zone non remblayée de Rotterdam, aux Pays-Bas. *Modification de l'Environnement de Réglementation* **14**, 895–908.

Nsangou, D., Kpoumié, A., Mfonka, Z., Bateni, S., Ngouh, A. & Ndam Ngoupayou, J. 2022 The Mfoundi watershed at Yaounde in the humid tropical zone of Cameroon: A case study of urban flood susceptibility mapping. *Earth Systems and Environment* **6**, 99–120. doi:10.1007/s41748-021-00276-9.

Pradhan, B. & Youssef, A. 2011 Cartographie de la susceptibilité aux crues maximales sur 100 ans à l'aide de modèles hydrologiques et hydrodynamiques intégrés : Couloir de la rivière Kelantan, Malaisie. *Gestion des Risques d'Inondation* **4**, 189–202.

Pradhan, B., Hagemann, U., Tehrany, M. & Prechtel, N. 2014 An easy to use ArcMap based texture analysis program for extraction of flooded areas from TerraSAR-X satellite image. *Comput. Geosci.* **63**, 34–43.

Rahmati, O., Pourghasemi, H. & Zeinivand, H. 2016 Flood susceptibility mapping using frequency ratio and weights-of-evidence models in the Golastan Province, Iran. *Geocarto International.* doi:10.1080/10106049.2015.1041559.

Samanta, S., Pal, D. K. & Palsamanta, B. 2018 Flood susceptibility analysis through remote sensing GIS and frequency ratio model. *Applied Water Science* **8**, 66.

Sone, E. W., Onguéné, R., Ndongo, B., Nshagali, G., Colmet-Daage, A., Marie, G., Iroumé, J., Stieglitz, T., Besck, F., Efole Ewoukem, T., Tomedi Eyango, M., Etamé, J. & Braun, J. J. 2023 Using GIS and multicriteria analysis to map flood risk areas of the Tongo Bassa River Basin (Douala, Cameroon). *Journal of Coastal Research* **39** (3), 531–543. doi:10.2112/JCOASTRES-D-22-00019.1.

Stefanidis, S. & Stathis, D. 2013 Evaluation des risques d'inondation basée sur des facteurs naturels et anthropiques à l'aide du processus de hiérarchie analytique (AHP). *Nature Hazards* **68**, 569–585.

Strobl, R. O., Forte, F. & Lonigro, T. 2012 Comparaison de la faisabilité de trois techniques de délimitation de l'étendue des risques d'inondation à l'aide du système d'information géographique: Étude de cas à Tavoliere delle Puglie, Italie. *Gestion des Risques d'Inondation* **5**, 245–257.

Tehrany, M. S., Pradhan, B. & Jebur, M. N. 2015 Flood susceptibility analysis and its verification using a novel ensemble support vector machine and frequency ratio method. *Stochastic Environmental Research and Risk Assessment* **29**, 1149–1165. doi:10.1007/s00477-015-1021-9.

UN. 2018 *World Urbanization Prospects 2018, New York: United Nations Department of Economic and Social Affairs (UN-DESA), Population Division. May (16) Retrieved From United Nations Department of Economic and Social Affairs.*

Vidhee, A. & Amit, G. 2020 Implications of land use transitions and climate change on local flooding in urban areas: An assessment of 42 Indian cities. *Land Use Policy* **95**, 104571. doi:10.1016/jlandusepol.2020.104571.

Zou, Q., Zhou, J., Zhou, C., Song, L. & Guo, J. 2013 Comprehensive flood risk assessment based on set pair analysis-variable fuzzy sets model and fuzzy AHP. *Stochastic Environmental Research and Risk Assessment* **27** (2), 525–546.

First received 8 September 2023; accepted in revised form 5 March 2024. Available online 18 March 2024